Spin, charge, and orbital ordering in the ferrimagnetic insulator $YBaMn_2O_5$

R. Vidya,* P. Ravindran, A. Kjekshus, and H. Fjellvåg
Department of Chemistry, University of Oslo, Box 1033, Blindern, N-0315 Oslo, Norway
(Received 4 May 2001; published 29 March 2002)

The oxygen-deficient (double) perovskite $YBaMn_2O_5$, containing corner-linked MnO_5 square pyramids, is found to exhibit ferrimagnetic ordering in its ground state. In the present work we report generalized-gradient-corrected, relativistic first-principles full-potential density-functional calculations performed on $YBaMn_2O_5$ in the paramagnetic, ferromagnetic, and ferrimagnetic states. The charge, orbital, and spin orderings are explained with site-, spin-, angular-momentum-, and orbital-projected density of states, charge-density plots, electronic structure, and total energy studies. $YBaMn_2O_5$ is found to stabilize in a *G*-type ferrimagnetic state in accordance with experimental results. The experimentally observed semiconducting behavior appears only when we include ferrimagnetic ordering in our calculation. We observed significant optical anisotropy in this material originating from the combined effect of ferrimagnetic ordering and crystal-field splitting. In order to gain knowledge about the presence of different valence states for Mn in $YBaMn_2O_5$ we have calculated *K*-edge x-ray absorption near-edge spectra for the Mn and O atoms. The presence of the different valence states for Mn is clearly established from the x-ray absorption near-edge spectra, hyperfine field parameters, and the magnetic properties study. Among the experimentally proposed structures, the recently reported description based on $P4/nmm$ is found to represent the stable structure.

DOI: 10.1103/PhysRevB.65.144422 PACS number(s): 75.50.Gg, 75.30.−m, 71.20.−b, 78.20.Ci

I. INTRODUCTION

Perovskite-type transition-metal oxides ABO_3 and their oxygen-deficient relatives exhibit a variety of interesting physical properties including high-temperature superconductivity, metal-insulator transition, and a variety of cooperative magnetic phenomena. Among them manganites have recently attracted particular attention because of the discovery of colossal negative magnetoresistance (CMR) in $La_{1-x}Sr_xMnO_3$,[1] $La_{1-x}Ba_xMnO_3$,[1] and related phases.[2–5] This renewed interest in the mixed-valence manganese perovskites such as $La_{1-x}Pb_xMnO_3$ is due to their potential technological applications.[6,7] In addition, the search for new high-temperature superconductors in mixed-oxide materials is a driving force for attention. The mechanism of high-temperature superconductivity is believed to be linked to cooperative interaction between copper $3d_{x^2-y^2}$ and $3d_{z^2}$ orbitals and oxygen $2p$ orbitals.[8] An attractive approach to obtain insight into the nature of this phenomenon is to examine the magnetic and electrical properties of non-copper-oxide analogues of known high-temperature superconducting cuprates. Manganese is a good choice for such a task, as in an octahedral perovskite-like configuration, Mn^{3+} (d^4 high spin with a single electron in an e_g orbital) will experience a similar Jahn-Teller (JT) distortion to that of Cu^{2+} [d^9 high spin with three electrons (or one hole) in the e_g orbitals]. The hole-doped manganese perovskites show some similarities to the corresponding hole-doped Cu phases in which superconductivity occurs.[9] Structural similarities between these two groups of materials suggest that new Mn analogs of the high-temperature superconducting Cu oxides may be prepared.

Since the discovery of CMR phenomena in perovskite-related manganites, extensive studies have been performed on manganese oxides with atomic arrangements related to the perovskite and pyrochlore structures over a wide variety of compositions with the aim to explore exotic spin-charge-coupled states.[10] Anisotropic CMR phenomena have also recently been reported in layered Ruddlesden-Popper variants of perovskites $(R,A)_{n+1}Mn_nO_{3n+1}$ (R=rare earth, A=alkaline earth) for $n=2$.[11] Similar effects have also been observed in the oxygen-deficient cubic pyrochlore $Tl_2Mn_2O_{7-\delta}$. The chemical features common to these materials are an intimately connected Mn-O-Mn network, within a three-dimensional or multilayered structure, and an average Mn oxidation state between $3+$ and $4+$ (obtained by hole-doping of Mn^{3+}).[12]

At low temperatures, manganese perovskites are characterized by the strong competition between charge-carrier itinerancy and localization. In the former case a ferromagnetic (F) metallic state is formed. In the latter case, the localized carriers tend to form charge-ordered (CO) states, which have a predominantly antiferromagnetic (AF) insulating character. Hence, we have a competition between F with metallic behavior and cooperative JT distortion with CO. The CO state can be converted into an F metallic state by the application of a magnetic field. The intriguing doping-induced, temperature-dependent metal-insulator transition and the interwoven magnetic (spin-), orbital-, and charge-ordering phenomena in mixed-valence manganese perovskites and transition-metal oxides have attracted much attention in recent years.[13] An active role of the orbital degree of freedom in the lattice and electronic response can be most typically seen in manganese perovskite oxides. As a matter of fact such properties appear to have their origin in the unique electronic structures derived from the hybridized Mn $3d$ and O $2p$ orbitals in the particular structural and chemical environment of a perovskite. The thus resulting intra-atomic exchange and the orbital degrees of freedom of the Mn $3d$ electrons play essential roles in this constellation. Furthermore, various kinds of structural distortion profoundly influence the electronic properties. The extensive studies of CMR in $R_{1-x}A_xMnO_3$ have brought forth novel features related to

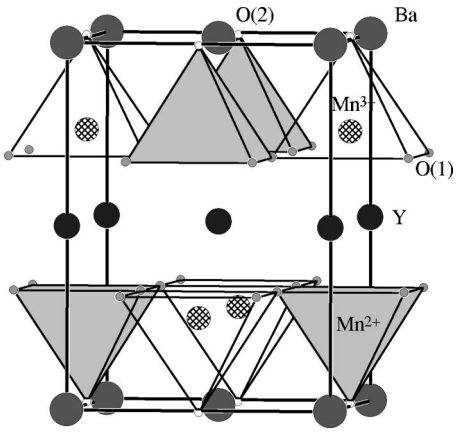

FIG. 1. The $YBaMn_2O_5$ crystal structure. The Y and Ba ions form layers along *c*. The square pyramids corresponding to Mn^{3+} and Mn^{2+} are shown by open and shaded polyhedra, respectively. The O atoms at the bases and apices of the square pyramids are denoted O(1) and O(2), respectively.

CO in these oxides. In transition-metal oxides with their anisotropic-shaped *d* orbitals, the Coulomb interaction between the electrons (strong electron correlation effect) may be of great importance. Orbital ordering (OO) gives rise to anisotropic interactions in the electron-transfer process which in turn favors or disfavors the double-exchange and the superexchange (F or AF) interactions in an orbital direction-dependent manner and hence gives a complex spin-orbital-coupled state. OO in the manganese oxides occasionally accompanies the concomitant CO.[14] The ordered oxygen-deficient double perovskites $RBaT_2O_{5+\delta}$ (T=transition metals like Fe, Co, and Mn) have attracted much attention as new spin-charge-orbital-coupled systems and new CMR materials. In the isostructural phases with R =Gd and Eu CMR effects of some 40% are observed.[15] As the experimental findings have been made available only in recent years, little theoretical work has been undertaken to understand the origin of these microscopic properties. The present study reports a detailed theoretical investigation of the electronic structure and optical properties of $YBaMn_2O_5$.

At low temperature, $YBaMn_2O_5$ is an AF insulator with CO of Mn^{3+} and Mn^{2+} accompanied by OO and spin ordering (SO).[25] The mechanism of CO and SO in manganites is not at all clear. Different authors have emphasized the importance of different ingredients such as on-site Coulomb interactions,[16–18] JT distortion,[19,20] and intersite Coulomb interactions.[21] Therefore, we have attempted to study CO, OO, and SO through full-potential linear muffin-tin orbital (FPLMTO) and full-potential linear augmented plane-wave (FPLAPW) methods. Similar to Fe_3O_4 and $SmBaFe_2O_{5+w}$ where Fe takes the conventional valence states of Fe^{3+} and Fe^{2+} at low temperature,[22,23] Mn is reported to occur as Mn^{3+} and Mn^{2+} in $YBaMn_2O_5$. Above the so-called Verwey temperature (T_V) valence-state mixing has been observed in Fe_3O_4 as well as in $SmBaFe_2O_{5+w}$. This brings in an additional interesting aspect in the study of the electronic structure and magnetic properties of Mn in $YBaMn_2O_5$. The first structural determinations based on powder x-ray (300 K) (Ref. 12) and neutron (100–300 K) (Ref. 24) diffraction data found that $YBaMn_2O_5$ crystallizes in space group $P4/mmm$, whereas a more recent powder neutron (2–300 K) (Ref. 25) diffraction (PND) study found $P4/nmm$. So a theoretical examination of the total energy for the two different structural alternatives is required.

The rest of the paper is arranged as follows: Section II gives crystal structure details for $YBaMn_2O_5$. The theoretical methods used for the calculations are described in Sec. III. The analysis of the band structure is given in Sec. IV A. Section IV B deals with the nature of the chemical bonding in $YBaMn_2O_5$, analyzed with the help of site-, spin-, angular-momentum-, and orbital-projected density of states (DOS). Section IV C discusses CO and OO in $YBaMn_2O_5$ with the help of charge-density plots. The results from calculations of optical spectra and x-ray absorption near-edge (XANE) spectra are discussed in Secs. IV D and IV E, respectively. Section IV F deals with hyperfine parameters. Finally the important conclusions are summarized in Sec. V.

II. CRYSTAL STRUCTURE

Chapman *et al.*[12] synthesized rather impure $YBaMn_2O_5$ and reported the crystal structure parameters according to space group $P4/mmm$ (described as double or ordered, oxygen-deficient perovskite, closely related to $YBaCuFeO_5$). These findings were subsequently confirmed by McAllister and Attfield[24] who also established a model for the ferrimagnetic ordering of the magnetic moments of Mn in $YBaMn_2O_5$ (still based on an impure sample). More recently Millange *et al.*[25] have succeeded in preparing phase-pure $YBaMn_2O_5$ and these authors report crystal and magnetic structure parameters according to space group $P4/nmm$.

Within the $P4/nmm$ description $YBaMn_2O_5$ crystallizes with $a=5.5359$ and $c=7.6151$ Å; Y in $2(b)$, Ba in $2(a)$, Mn(1) in $2(c)$ with $z=0.2745$, Mn(2) in $2(c)$ with $z=0.7457$, O(1) in $8(j)$ with $x=0.4911$, $y=0.9911$, and $z=0.4911$, and O(2) in $2(c)$ with $z=0.0061$. The lacking oxygens in the yttrium plane, compared with the perovskite-aristotype structure, reduces the coordination number of yttrium to 8, while barium retains the typical 12 coordination of the perovskite structure. The Mn-O network consists of double layers of MnO_5 square pyramids, corner shared in the ab plane and linked via their apices.

According to the $P4/nmm$ description (Fig. 1) the two kinds of MnO_5 pyramids are arranged in an ordered manner, each $Mn^{2+}O_5$ pyramid being linked to five $Mn^{3+}O_5$ pyramids. Owing to this charge ordering, each Mn^{2+} has four Mn^{3+} in-plane neighbors. Oxygen takes two crystallographically different sites. O(1) forms the base of the square pyramids, while O(2) is located at the apex of the pyramids. The interatomic Mn-O distances fall in four categories, being 1.908 and 2.086 Å for Mn^{3+}-O(1) and Mn^{2+}-O(1), respectively, whereas O(2) is 2.081 and 1.961 Å away from Mn^{3+} and Mn^{2+}, respectively. (The $P4/mmm$ description gave on the other hand, almost equal basal and apical Mn-O distances within all square pyramids.[12]) The basal plane Mn^{3+}-O(1)-Mn^{2+} angle is 157.8° and the apical Mn^{3+}-O(2)-Mn^{2+} angle is 180°. The large variation in these angles play a key role in the magnetic properties.

III. COMPUTATIONAL DETAILS

A. FPLMTO computations

The present calculations have used the FPLMTO method[26] where no shape approximation is assumed for the one-electron potential and charge density. The basis geometry consists of muffin-tin (MT) spheres centered around the atomic sites with an interstitial region in between. Inside the MT spheres the charge density and potential are expanded by means of spherical harmonic functions multiplied by a radial component. The interstitial basis function is a Bloch sum of linear combinations of Neumann or Henkel functions depending on the sign of the kinetic energy κ^2 (corresponding to the basis functions in the interstitial region). Each Neumann or Henkel function is then augmented (replaced) by a numerical basis function inside the MT spheres, in the standard way of the linear MT orbital method.[27] Since a Bloch sum of atomic centered Henkel or Neumann functions has the periodicity of the underlying lattice it may be expanded in a Fourier series, as done here. The spherical-harmonic expansion of the charge density, potential, and basis functions was performed up to $l_{max}=6$. The basis included Y $4p$, $5s$, $5p$, and $4d$ states, Ba $5p$, $6s$, $6p$, $5d$, and $4f$ states, Mn $4s$, $4p$, and $3d$ states, and O $2s$, $2p$, and $3d$ states.

Furthermore, the calculations are all electron as well as fully relativistic. The latter level is obtained by including the mass velocity and Darwin (and higher-order) terms in the derivation of the radial functions (inside the MT spheres) whereas the spin-orbit coupling was included at the variational step using an (l,s) basis. Moreover, the present calculations made use of a so-called double basis, to ensure a well-converged wave function. This means that two Neumann or Henkel functions were applied, each attached to its own radial function with an (n,l) quantum number. The integrations over the Brillouin zone (BZ) in the ground-state calculations were performed as a weighted sum, using the special point sampling,[28] with weights reflecting the symmetry of a given **k** point. We also used a Gaussian smearing width of 20 mRy for each eigenvalue in the vicinity of the Fermi level to speed up the convergence. For the DOS and optical calculations, the tetrahedron integration was employed. The calculations were performed for the experimentally determined structural parameters (see Sec. II). For the exchange-correlation functional $E_{xc}(n)$, we have used the generalized gradient approximation (GGA) where the gradient of the electron density is taken into account using the Perdew and Wang[29] implementation of the GGA. Here 192 **k** points in the irreducible part of the primitive tetragonal BZ were used for the self-consistent ground-state calculations and 352 **k** points for the optical calculations.

B. FPLAPW computations

For the XANES and orbital-projected DOS calculations we have applied the FPLAPW method[30] in a scalar-relativistic version without spin-orbit coupling. The FPLAPW method divides space into an interstitial region (IR) and nonoverlapping MT spheres centered at the atomic sites. In the IR, the basis set consists of plane waves. Inside the MT spheres, the basis set is described by radial solutions of the one-particle Schrödinger equation (at fixed energies) and their energy derivatives multiplied by spherical harmonics. The charge densities and potentials in the atomic spheres were represented by spherical harmonics up to $l=6$, whereas in the interstitial region these quantities were expanded in a Fourier series with 3334 stars of the reciprocal lattice vectors **G**. The radial basis functions of each LAPW were calculated up to $l=10$ and the nonspherical potential contribution to the Hamiltonian matrix had an upper limit of $l=4$. Atomic-sphere radii R_{MT} of 2.5, 2.8, 1.8, and 1.6 a.u. for Y, Ba, Mn, and O, respectively, were used. Since the spin densities are well confined within a radius of about 1.5 a.u, the resulting magnetic moments do not depend appreciably with the chosen atomic-sphere radii. The initial basis set included $5s$, $5p$, and $4d$ valence and $4s$ and $4p$ semicore functions for Y, $6s$, $6p$, and $6d$ valence and $5s$ and $5p$ semicore functions for Ba, $4s$, $4p$, and $3d$ valence and $3s$ and $3p$ semicore functions for Mn and $2s$, $2p$, and $3d$ functions for O. These basis functions were supplemented with local orbitals[31] for additional flexibility to the representation of the semicore states and for generalization of relaxation of the linearization errors. Owing to the linearization errors DOS are reliable only to about 1–2 Ry above E_F. Therefore, after self-consistency was achieved for this basis set we included higher-energy local orbitals: $5d$- and $4f$-like functions for Y, $6d$- and $4f$-like functions for Ba, $5s$- and $5p$-like functions for Mn, and $3p$-like functions for O. The BZ integration was done with a modified tetrahedron method[32] and we used 140 **k** points in the irreducible wedge of BZ. Exchange and correlation effects are treated within density-functional theory (DFT), using the GGA.[29]

C. Optical properties

Optical properties of matter can be described by means of the transverse dielectric function $\epsilon(\mathbf{q},\omega)$ where **q** is the momentum transfer in the photon-electron interaction and ω is the energy transfer. At lower energies one can set $\mathbf{q}=\mathbf{0}$, and arrive at the electric dipole approximation, which is assumed throughout this paper. The real and imaginary parts of $\epsilon(\omega)$ are often referred to as ϵ_1 and ϵ_2, respectively. We have calculated the dielectric function for frequencies well above those of the phonons and therefore we considered only electronic excitations. In condensed matter systems, there are two contributions to $\epsilon(\omega)$, viz., intraband and interband transitions. The contribution from intraband transitions is important only for metals. The interband transitions can further be split into direct and indirect transitions. The latter involves scattering of phonons and are neglected here, and moreover these only make small contribution to $\epsilon(\omega)$ in comparison to the direct transitions,[33] but have a temperature broadening effect. Also other effects, e.g., excitons (which normally give rise to rather sharp peaks), affect the optical properties.

The direct interband contribution to the imaginary part of the dielectric function $\epsilon_2(\omega)$ is calculated by summing all possible transitions from occupied to unoccupied states, taking the appropriate transition-matrix element into account. The dielectric function is a tensor for which all components

TABLE I. Total energy in different magnetic configurations.

Type	Paramagnetic	Ferromagnetic	Antiferromagnetic
Total energy (Ry/f.u.)	−28438.0466	−28438.2754	−28438.3125
ΔE (meV/f.u.)	3618.6	505.6	0.0
Electronic state	Metal	Metal	Semiconductor
		Calculated magnetic moment (μ_B)	
	Ferromagnetic	Antiferromagnetic	Experimental[a]
Mn^{3+}	3.45	3.07	2.91
Mn^{2+}	3.99	3.93	3.91
Saturated	7.44	0.86	0.95

[a]Reference 25.

are needed for a complete description. However, we restrict our considerations to the diagonal matrix elements $\epsilon^{\nu\nu}(\omega)$ with $\nu=x$, y, or z. The interband contribution to the diagonal elements of $\epsilon_2(\omega)$ is given by

$$\epsilon_2^{\nu\nu}=\frac{8\pi^2e^2}{m^2\omega^2}\sum_{n}^{unocc}\sum_{n'}^{occ}\int_{BZ}|P^{\nu}_{nn'}(k)|^2 f_{kn}(1-f_{kn'})\times\delta(E^k_n-E^k_{n'}-\hbar\omega)\frac{d^3k}{(2\pi)^3}, \quad (1)$$

where e is the electron charge, m its mass, f_{kn} the Fermi-Dirac distribution function, $P^{\nu}_{nn'}$ the projection of the momentum matrix elements along the direction ν of the electric field, and E^k_n one-electron energies. The evaluation of the matrix elements in Eq. (1) is done separately over the MT and interstitial regions. Further details about the evaluation of matrix elements are found in Ref. 34. The integration over BZ in Eq. (1) is performed using linear interpolation on a mesh of uniformly distributed points, i.e., the tetrahedron method. The total $\epsilon_2^{\nu\nu}$ was obtained from $\epsilon_2^{\nu\nu}$(IBZ); i.e., $\epsilon_2^{\nu\nu}$ was calculated only for the irreducible (I) part of the BZ using

$$\epsilon_2(\omega)=\frac{1}{N}\sum_{i=1}^{N}\sigma_i^T\epsilon_2(\mathrm{IBZ})\sigma_i, \quad (2)$$

where N is the number of symmetry operations and σ_i represents the symmetry operations; for shortness, $\epsilon(\omega)$ is used instead of $\epsilon^{\nu\nu}(\omega)$. Lifetime broadening was simulated by convoluting the absorptive part of the dielectric function with a Lorentzian, whose full width at half maximum (FWHM) is equal to $0.005(\hbar\omega)^2$ eV. The experimental resolution was simulated by broadening the final spectra with a Gaussian of constant FWHM equal to 0.01 eV.

After having evaluated Eq. (2) we calculated the interband contribution to the real part of the dielectric function $\epsilon_1(\omega)$ from the Kramers-Kronig relation

$$\epsilon_1(\omega)=1+\frac{2}{\pi}P\int_0^{\infty}\frac{\epsilon_2(\omega')\omega' d\omega'}{\omega'^2-\omega^2}. \quad (3)$$

In order to calculate $\epsilon_1(\omega)$ one needs a good representation of $\epsilon_2(\omega)$ up to high energies. In the present work we have calculated $\epsilon_2(\omega)$ up to 41 eV above the E_F level, which also was the truncation energy used in Eq. (3).

To compare our theoretical results with the experimental spectra we have calculated polarized reflectivity spectra using the following relation. The specular reflectivity can be obtained from the complex dielectric constant in Eq. (1) through the Fresnel's equation

$$R^{\nu\nu}(\omega)=\left|\frac{\sqrt{\epsilon(\omega)}-1}{\sqrt{\epsilon(\omega)}+1}\right|^2. \quad (4)$$

We have also calculated the absorption coefficient $I(\omega)$ and the refractive index n using the following expressions:

$$I(\omega)=2\omega\left[\frac{(\epsilon_1^2(\omega)+\epsilon_2^2(\omega))^{1/2}-\epsilon_1(\omega)}{2}\right]^{1/2} \quad (5)$$

and

$$n=\left[\frac{\sqrt{\epsilon_1^2+\epsilon_2^2}+\epsilon_1}{2}\right]^{1/2}. \quad (6)$$

IV. RESULTS AND DISCUSSION

A. Electronic band structure

The FPLMTO calculations were performed on $YBaMn_2O_5$ for three different magnetic configurations, viz., paramagnetic (P), ferromagnetic (F), and antiferromagnetic (AF). From Table I it can be seen that in the AF configuration, the spins are not canceled and hence this state is really ferrimagnetic (Ferri). Moreover, Table I shows that Ferri $YBaMn_2O_5$ has lower energy than the P and F configurations. The energy-band structure of Ferri $YBaMn_2O_5$ is shown in Figs. 2(a) and 2(b) for up- and down-spin bands, respectively. $YBaMn_2O_5$ is seen to be an indirect-band-gap semiconductor. A closer inspection of the energy-band structure shows that the band gap is between the top of the valence band (VB) at the Γ point and the bottom of the conduction band (CB) at the Z point. As the unit cell contains 18 atoms, the band structure is quite complicated and Fig. 2 therefore only depicts the energy range −7.5–7.5 eV.

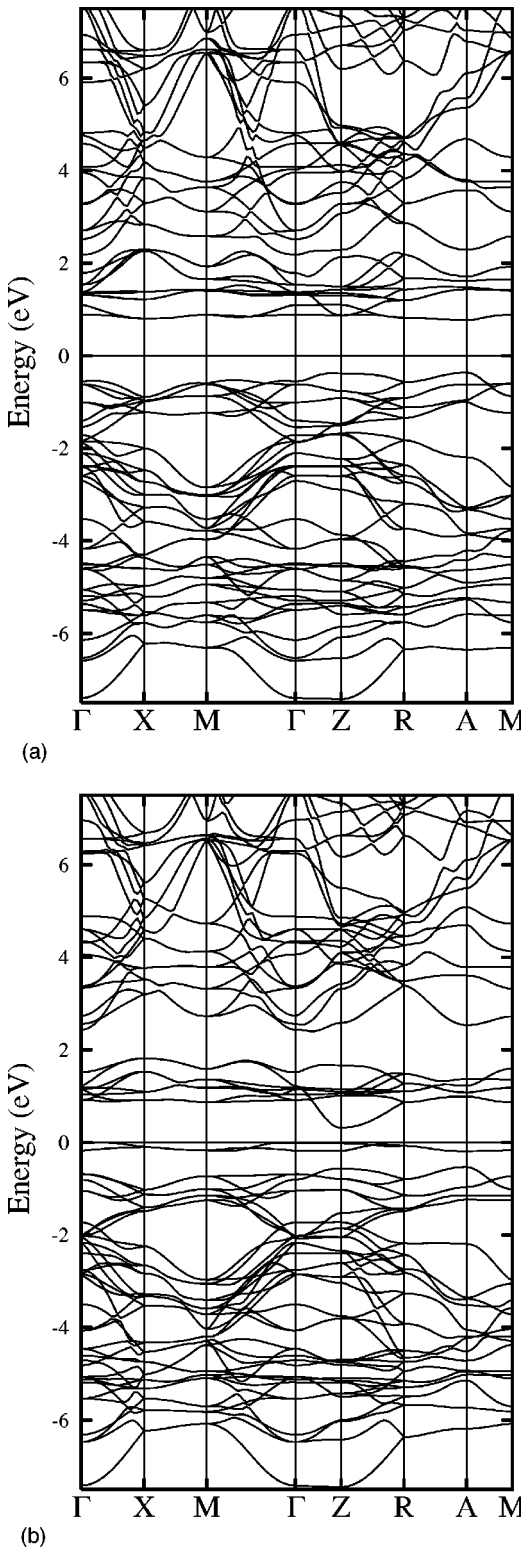

FIG. 2. The electronic band structure of $YBaMn_2O_5$ in the antiferromagnetic state: (a) up-spin bands and (b) down-spin bands. The line at 0 eV refers to the Fermi energy level.

There is a finite energy gap of 1.307 eV between the topmost-occupied VB and the bottommost-unoccupied CB in the up-spin channel. For the purpose of more clarity, it is convenient to divide the occupied portion of the band structure in the up-spin channel into three energy regions: (i) bands lying at and below -4 eV, (ii) bands lying between -4 and -2 eV, and (iii) the top of the VB, closer to E_F, viz., the range -2–0 eV. Region (i) contains 17 bands with contributions from Y $4s$, $5s$, Mn $3s$, $3d$, and O $2p$ electrons. Region (ii) comprises bands which originate from completely filled O(1) and O(2) $2p$ orbitals. Region (iii) includes 10 bands. Among them one finds delocalized (dispersed) bands originating from Y $5s$ and O $2p$ orbitals and somewhat localized bands attributed to Mn(1) d_{z^2}, $d_{x^2-y^2}$, d_{xz}, and d_{yz} orbitals. The topmost-occupied band contains electrons stemming from the Mn d_{z^2} orbital. In the unoccupied portion of the band structure, a corresponding division leads to two energy regions: (1) The bottommost CB from 0 to 2 eV and (2) the middle range of CB from 2 to 4 eV. (Above 4 eV the bands are highly dispersed and it is quite difficult to establish the origin of the bands.) There are 9 bands in region (1) which have some Y $5s$, Ba $5d$, Mn(1) $3d_{xy}$, and Mn(2) $3d$ characters. In region (2) the bands retain Y $6s$ and $4d$, Ba $7s$ and $5d$, and Mn $4s$, $4p$, and $3d$ characters.

The energy-band structure of the down-spin channel [Fig. 2(b)] has 16 bands in the region (i) up to -4 eV which arise from the *s* and *p* electrons of the Y, Ba, Mn, and O atoms. The mainly *s*- and *p*-electron character of the bands makes them appreciably dispersed. The second energy region (ii) contains 12 bands, which have Y $5s$, Ba $5p$, Mn(2) $3d$, and O(1), O(2) $2p$ character. The third region (iii) closer to E_F has 10 bands which are mainly arising from Mn(1), Mn(2) $3d$, and O(1), O(2) $2p$ orbitals. Unlike the up-spin channel the down-spin channel contains two bands at E_F which arise from the originally half-filled d_{yz}, d_{xz} orbitals of Mn(1) and the half-filled d_{xy} orbital of Mn(2).

A finite band gap of 1.046 eV opens up between the highest-occupied VB and bottommost-unoccupied CB. The unoccupied portion of the down-spin channel is quite different from that of the up-spin channel. The lowest-lying unoccupied band has Mn(2) $4s$ electrons. Between 0 and 2 eV there are 8 bands which arise mainly from Mn(1) $3d$ electrons as well as from Mn(1) and Mn(2) $4s$ electrons and O(1) and O(2) $2p$ electrons. The dispersed bands present between 2 and 4 eV have Y $5s$ and $3d$, Ba $6s$ and $5d$, and Mn(1) $3d$ characters.

B. DOS characteristics

In order to theoretically verify which of the two ($P4/mmm$ or $P4/nmm$ based) structures is energetically more stable, we performed first-principles calculations for both variants. The calculated DOS value at E_F for the P phase $P4/mmm$ variant is 192.82 states/(Ry f.u.) and for $P4/nmm$ 149 states/(Ry f.u.) in the P state. Hence, a larger number of electrons are present at E_F for the former variant, which favors the relative structural stability of the latter. Moreover, our calculations show that the $P4/nmm$ variant is 860 meV/f.u. lower in energy than the $P4/mmm$ variant. Therefore we conclude that $YBaMn_2O_5$ is more stable in space group $P4/nmm$ than in $P4/mmm$, viz., in accordance with the most recent PND-based experimental study.

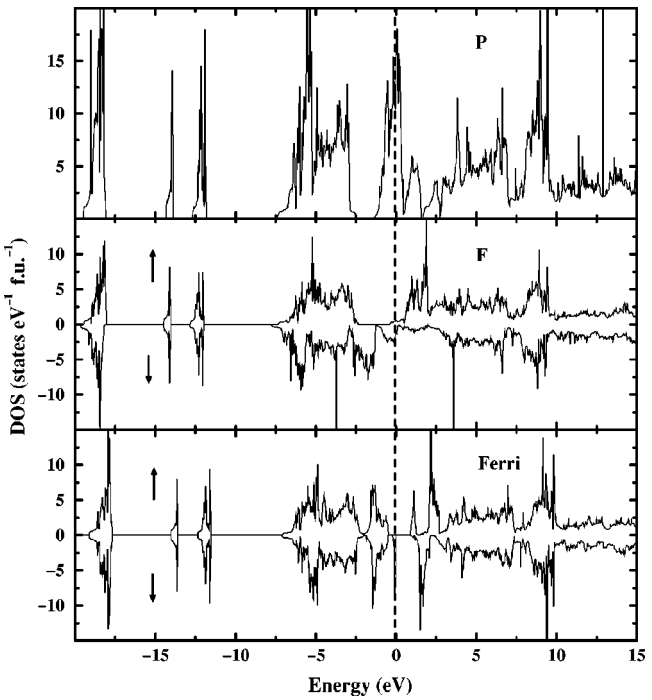

FIG. 3. Total density of states (DOS) for $YBaMn_2O_5$ in para-, ferro-, and ferrimagnetic states.

Our calculated total DOS curves for $YBaMn_2O_5$ in the P, F, and Ferri configurations are given in Fig. 3. The highest-occupied energy level in the VB, i.e., E_F, is marked by the dotted line. In the P and F cases finite DOS values are present in the vicinity of E_F. Hence, both the P and F configurations exhibit metallic character. On going from the P to F case, the electrons start to localize which is seen from the reduced number of states at E_F. Due to the electron localization, a gain in total energy of 3.1 eV (Table I) is observed when the spin polarization is included in our calculations. However, in the Ferri case, a finite band gap of 0.88 eV opens up between the top of the VB and the bottom of the CB. The experimental studies also show semiconducting behavior.[12,35] From Table I it can be seen that the Ferri configuration has lower energy than the other two configurations. The present observation of the stabilization of a Ferri ground state in $YBaMn_2O_5$ is consistent with the established magnetic structure.[25] It is interesting to note that the introduction of the Ferri configuration is essential in order to obtain the correct semiconducting state for $YBaMn_2O_5$. Unlike $LaMnO_3$ (where the energy difference between the F and AF cases is ~ 25 meV),[36] there is a large energy difference (~ 0.5 eV) between the Ferri and the F states of $YBaMn_2O_5$. So a very large magnetic field is required to stabilize the F phase and induce insulator-to-metal transition in $YBaMn_2O_5$.

In the $RMnO_3$ phases hole doping induces CE-type magnetic ordering in which the spins are F aligned in zigzag chains with AF coupling between these chains. In $YBaMn_2O_5$, the Mn spins are AF aligned within quasi-one-dimensional chains as well as between the chains. The main difference between $YBaMn_2O_5$ and $RMnO_3$ is that the latter have e_g electrons present in the vicinity of E_F and that the

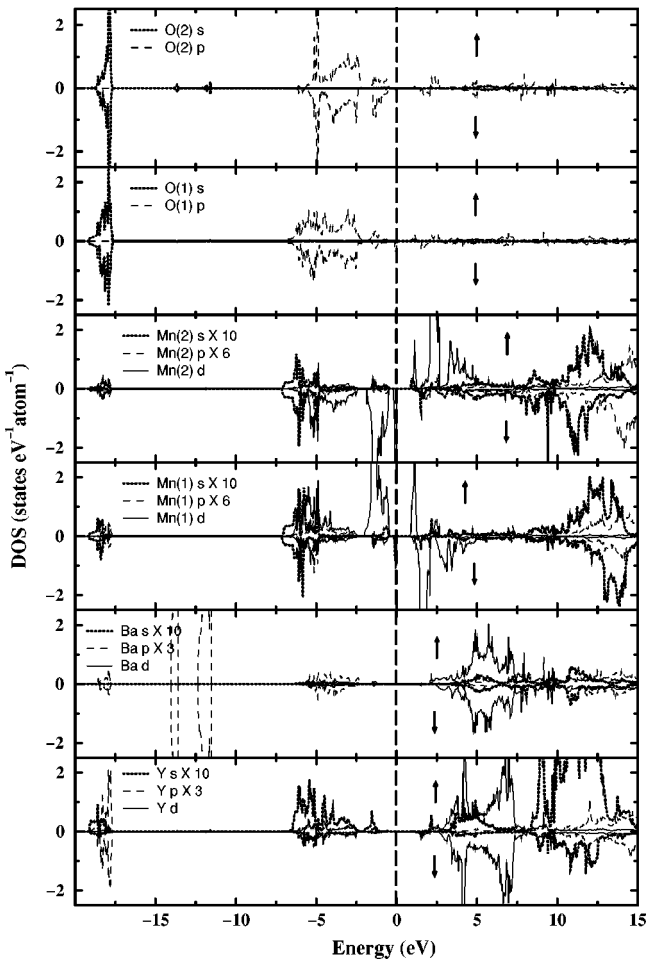

FIG. 4. Site-, spin-, and angular-momentum-decomposed DOS of $YBaMn_2O_5$ in the ferrimagnetic state, obtained by the full-potential LMTO method.

superexchange interaction originates from the localized t_{2g} electrons. Owing to the square-pyramidal crystal field in $YBaMn_2O_5$ both e_g (d_{xy} and d_{z^2} DOS in local coordinates) and t_{2g} (d_{yz}, d_{xz}, and $d_{x^2-y^2}$ DOS in local coordinates) electrons (Fig. 5) get localized and hence both e_g and t_{2g} electrons participate in the superexchange interaction. This is the main reason why the F state has much higher energy than the AF state in $YBaMn_2O_5$ as compared with $LaMnO_3$.

To obtain more insight into the DOS features, we show the angular-momentum-, spin-, and site-decomposed DOS in Fig. 4. The lower panels for Y and Ba show that, in spite of the high atomic numbers for Y and Ba, small DOS values are seen in VB. The Y and Ba states come high up in CB (ca. 4 eV above E_F), indicating a nearly total ionization of these atoms. They lose their valence charge to form ionic bonding with oxygen. According to the crystal structure, Y and Ba are located in layers along *c*, which is clearly reflected in the electronic charge-density distribution within (100) in the AF configuration (Fig. 6).

The distinction between Mn(1) and Mn(2) is clearly reflected in the different topology of their DOS curves. As seen from Table I, Mn(1) has a smaller magnetic moment

($3.07\mu_B$) than Mn(2) ($3.91\mu_B$) which leads to the conclusion that Mn(1) corresponds to Mn^{3+} and Mn(2) to Mn^{2+}, both in high-spin states. Both Mn(1) and Mn(2) have low-lying DOS features around -17 eV which can be attributed to well-localized *s* and *p* electrons originating from the covalent interaction between Mn $3d$ with O $2s$ and $2p$ states. The somewhat dispersed DOS in the energy region -7.5 to -2.5 eV is attributed to $3d$ electrons for both Mn(1) and Mn(2). As Mn(1) and Mn(2) are AF coupled, their *d*-orbital DOS have opposite character. The localized peaks closer to E_F, with a width of about 2 eV, have both ($3d$) e_g and t_{2g} character (see below).

The top two panels of Fig. 4 show DOS for O(1) and O(2). Crystallographically O(1) is almost coplanar (in ab) with Mn, whereas O(2) is at the apex of the square pyramid (along c). The well-localized peaks in DOS for O(1) and O(2) at about -18 eV reflect the completely filled $2s$ orbitals. The spread-out DOS features between -7.5 and -0.5 eV are attributed to O $2p$ states. Figure 4 shows that the O $2p$ states are energetically degenerate with Mn $3d$ states in this energy range, implying that these orbitals form covalent bonds with Mn(1) and Mn(2) through hybridization. The presence of a strong covalent interaction between Mn and O in $YBaMn_2O_5$ is confirmed by our charge-density analysis. The almost empty DOS for O(1) and O(2) in the CB implies that the oxygen atoms are in nearly completely ionized states in $YBaMn_2O_5$.

In order to progress further in the understanding of the chemical bonding, charge, spin, and orbital ordering in $YBaMn_2O_5$, we have plotted the orbital-decomposed DOS for the $3d$ orbitals of Mn(1) and Mn(2) in Fig. 5. This illustration shows that DOS for the e_g orbitals (d_{z^2} and d_{xy}) for both Mn(1) and Mn(2) are well localized compared to that of Mn ions in $LaMnO_3$. There is a sharp peak at -5 eV in the up-spin panel for Mn(1) and in the down-spin panel for Mn(2) which correlates with a well-localized peak in DOS for O(2) (Fig. 4) This is attributed to the 180° Mn^{3+}-O(2)-Mn^{2+} bond angle which facilitates p-d σ bond to the O(2) p_z orbital and superexchange interaction.[37] As up-spin Mn(1) and down-spin Mn(2) are participating in the bonding, we infer that the superexchange interaction results in AF spin ordering between the Mn atoms involved. The peaks at ca. 1 eV in up-spin Mn(1) and down-spin Mn(2) are attributed to the (nonbonding) d_{z^2} orbitals.

Since the Mn atoms are surrounded by O atoms in a square-pyramidal arrangement and the Mn(1)-O(1)-Mn(2) bond angle is very much less than 180° (158°), the electron distributions in the e_g orbitals are very different. In particular the d_{z^2} electrons distributed closer to E_F and the d_{xy} electrons are well localized and nearly empty in the top of the VB. From Fig. 4, we see that the O $2p$ orbitals are also situated in the same energy range (-5 to 0 eV) as the d_{xy} orbitals of Mn(1) and Mn(2); thus, these orbitals and O(1) p_x and p_y orbitals form p-d σ bond. As the bond angle Mn(1)-O(1)-Mn2 is only 158°, the strength of this covalent bond is weak and consequently the AF superexchange interaction becomes weakened.[37] Despite the AF superexchange interaction, there is no exact cancellation of the spins of $Mn(1)^{3+}$ and $Mn(2)^{2+}$, and the result is a Ferri state with a finite magnetic moment of $0.85\mu_B$.

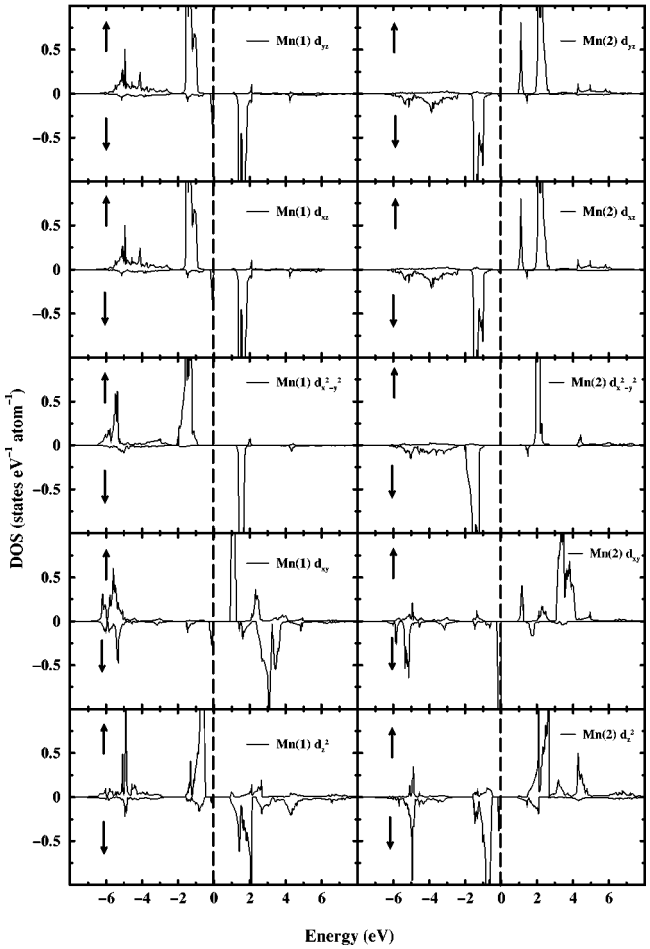

FIG. 5. Orbital (*d*) decomposed DOS for Mn(1) and Mn(2) in the ferrimagnetic state obtained by the full-potential FLAPW method.

Transition-metal perovskite oxides which exhibit CO like $La_{1-x}Sr_xMnO_3$ have an octahedral crystal field, whereas $YBaMn_2O_5$ has a square-pyramidal arrangement around Mn. In the former case, the t_{2g} electrons are in a well-localized state. But in $YBaMn_2O_5$ the t_{2g} electrons are closer to the E_F. Due to different nature of hybridization between the e_g orbitals and the O $2p$ state, they have a different DOS distribution as shown in Fig. 5. The t_{2g} orbitals (d_{yz}, d_{xz}, and $d_{x^2-y^2}$) of both Mn(1) and Mn(2) are energetically degenerate as clearly seen from the character of the DOS curve. The topology of orbital-projected DOS curves is similar for Mn(1) and Mn(2), except for the d_{xy} orbital. For Mn(1) the d_{xy} orbital has a very small peak at E_F whereas a finite-sized peak is observed for the same orbital of Mn(2). It is indeed the occupancy of this orbital which determines the magnetic moment of Mn(1) and Mn(2). If one considers the Goodenough-Kanamori[39] rules for magnetic interactions in manganese oxides, the expected magnetic order should be *A*-type AF (viz., F ordering within the layers and AF ordering between the layers, arising from superexchange interac-

tions between occupied d_{xy} orbitals on Mn^{2+} and empty d_{xy} on Mn^{3+}). However, owing to the large deviation of the Mn-O-Mn bond angle from 180° along with CO, the d_{xy} orbitals for both Mn species become occupied. Hence, AF ordering is observed between Mn within the planes as well as between the planes (see Fig. 7). One Mn couples AF to its six neighboring Mn in a *G*-type AF arrangement in accordance with experimental findings.[25] Hence, the theoretical calculations have provided the correct ground state with respect to the experiments.

Magnetic susceptibility and magnetization measurements have unequivocally shown that $YBaMn_2O_5$ is in a Ferri state at low temperature[12,25] with a saturated moment between $0.5\mu_B$ and $0.95\mu_B$ per $YBaMn_2O_5$ formula unit.[12,25] The theoretically calculated magnetic moments for Mn are $3.07\mu_B$ and $3.93\mu_B$, repectively, giving a net magnetic moment of $0.86\mu_B$ per formula unit for the Ferri state of $YBaMn_2O_5$. Our theoretically calculated value is less than the predicted (spin-only) value of $1.0\mu_B$. From the DOS analyses, we noted that there is strong hybridization between Mn $3d$ electrons and O $2p$ electrons. A finite magnetic moment of $0.0064\mu_B$/atom and $0.0032\mu_B$/atom are theoretically found to be present at O(1) and O(2), respectively. Hence, we conclude that the slight deviation in the saturated magnetic moment from that predicted by an idealized ionic model can be attributed to the strong hybridization between Mn $3d$ and O $2p$ electrons. We have also performed calculations with the room-temperature structural parameters, confirming that the two manganese atoms possess different magnetic moments at this temperature. In order to understand the role of JT distortion arising from the presence of Mn^{3+} ions in $YBaMn_2O_5$, it is interesting to study the lattice relaxation effect on the electronic structure and magnetic properties of this material. However, due to the intense computations involved in such studies, it is out of scope of the present investigation.

C. Charge and orbital ordering

For the pseudocubic and layered perovskite manganese oxides, essentially three parameters control the electron-correlation strength and the resultant structural, transport, and magnetic properties:[10] First, the hole-doping level (charge-carrier density or the band-filling level of the CB). In the case of perovskite oxides the substitution of a trivalent rare earth (*R*) by a divalent alkaline earth (*A*) introduces holes in the Mn $3d$ orbitals. Second, the effective one-electron bandwidth (*W*) or equivalently the e_g electron-transfer interaction. The magnitude of *W* is directly determined by the size of the atom at the *R* and *A* sites which makes the Mn-O-Mn bond angle deviate from 180° and thus hinders the electron-transfer interaction. The correlation between CO and the size of the *R* and *A* is studied by several workers and is well illustrated by a phase diagram in Ref. 40. Third comes the dimensionality: the lowering of the electronic dimensionality causes a variety of essential changes in the electronic properties. The carrier-to-lattice coupling is so strong in manganites that the charge-localization tendency becomes very strong. Investigations on the CO state have established an intimate connection to lattice distortion. It seems to be the lattice distortion associated with OO which localizes the charge and thus initiates CO.[40]

In general the ground state of mixed-valent manganite perovskites is either F and metallic or AF and CO. In all CO systems, the magnetic susceptibility drops rapidly at the CO temperature (T_{CO}). CO drastically influences the magnetic correlations in manganites. The effect of the CO state on cooperative magnetic states is to produce insulating behavior. A high magnetic field induces a meltinglike phenomenon of the electron lattice of the CO phase, giving rise to a huge negative magnetoresistance.[41] For these reasons, it is interesting to study CO in $YBaMn_2O_5$.

Charge localization, which is a prerequisite for CO, is mutually exclusive with an F state according to the double-exchange mechanism. The double-exchange mechanism requires hopping of charge carriers from one Mn to an adjacent Mn via an intervening O. The CO state is expected to become stable when the repulsive Coulomb interaction between carriers dominates over the kinetic energy of the carriers. Hence, CO arises because the carriers are localized at specific long-range-ordered sites below the CO temperature. CO is expected to be favored for equal proportions of Mn^{2+} and Mn^{3+} as in the present case, and in $YBaMn_2O_5$ it is associated with the AF coupling between Mn in the *ab* plane. CO depends on the *d*-electron bandwidth and hence it is worth to consider this feature in some detail. On reduction of the Mn-O-Mn angle, the hopping between the Mn $3d$ and O $2p$ orbital decreases and hence the e_g bandwidth decreases. Consequently the system stabilizes in a Ferri-CO-insulating state. Usually the CO-insulating state transforms to a metallic F state on the application of a magnetic field. This may be the reason for the metallic behavior of the F phase found in our calculation. CO in $YBaMn_2O_5$ is characterized by the real-space ordering of Mn^{2+} and Mn^{3+} species as shown in Figs. 6(a) and 6(b). Our calculations predict that a long-range CO of Mn^{2+} and Mn^{3+} with a rocksalt-type arrangement occurs at low temperatures. This can be viewed as chains of Mn^{2+} and Mn^{3+} running parallel to *b* and correspondingly alternating chains running along *a* and *c* (viz., a checkerboard arrangement of CO as seen from Fig. 7).

Furthermore, there exist orbital degrees of freedom for the Mn $3d$ electrons and OO can lower the electronic energy through the JT mechanism. Therefore, mixed-valent manganites can have OO in addition to CO.[42] OO gives rise to the anisotropy in the electron-transfer interaction. This favors or disfavors the double-exchange interaction and the (F or AF) superexchange interaction in an orbital-dependent manner and hence gives a complex spin-orbital-coupled state. Therefore, it is also interesting to study OO in some detail. Figures 6(a) and 6(b) show the electron charge density of $YBaMn_2O_5$ in *bc* (100) and *ab* (001) planes, respectively. As the electron-charge density is plotted in the energy range where the $3d$ orbitals reside, the shape of the d_{z^2} and $d_{x^2-y^2}$ orbitals are well reproduced in Figs. 6(a) and 6(b), respectively. The transfer integral between the two neighboring Mn atoms in the crystal lattice is determined by the overlap between the $3d$ orbitals with the $2p$ orbital of O atom. In the

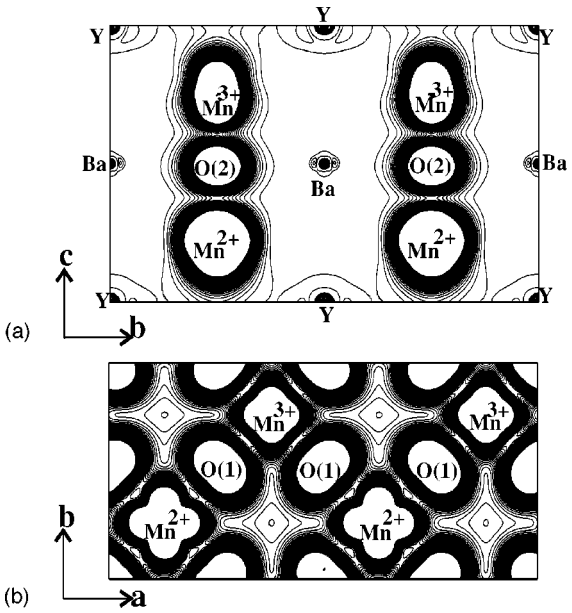

FIG. 6. Charge density distribution of $YBaMn_2O_5$ in (a) bc (100) and (b) ab (001) plane. Here 40 contours are drawn between 0 and 0.02 electrons/ a.u.^{3} The charge density is calculated in the energy range -4.57 eV to -3.42 eV in the bc plane and -9.37 eV to -3.82 eV in the ab plane in order to visualize the Mn $3d$ electrons.

bc plane the d_{z^2} orbital is ordered along c for both Mn(1) and Mn(2); this orbital hybridizes with the O(1) p_z orbital, resulting in a p-d σ bond. The finite electron density present within Mn(1)-O(2)-Mn(2) illuminates the path for the AF superexchange interaction between them. When the size of the R and A becomes smaller the one-electron bandwidth (or e_g electron-transfer interaction) decreases in value.[40] For Y^{3+} with an ionic radius of 1.25 Å [smaller than other R's like La^{3+} (1.36 Å) (Ref. 38)] the Mn(1)-O(1)-Mn(2) angle is much less than 180° so the e_g-electron bandwidth is small compared with the t_{2g}-electron bandwidth.

The overlap between the $d_{x^2-y^2}$ and p_z orbitals is zero because of their different orientation in the ab plane. Therefore, the electron in the $d_{x^2-y^2}$ orbital cannot hop along c.[37] Also the direct overlap between O $p_{x,y}$ and Mn d is minimal in the ab plane and hence the d electrons get localized and cause CO and OO. Owing to the fact that the Mn(1)-O(1) bond length is 1.908 Å compared with 2.086 Å for Mn(2)-O(1), more electronic charge is present on Mn^{2+} than on Mn^{3+}. This is visible in the orbital decomposed DOS (Fig. 5), where the d_{xy} orbital of Mn^{2+} has more states (electrons) than that of Mn^{3+}.

PND (Ref. 25) indicates that Mn^{3+} has the occupied d_{z^2} orbital extending along [001], whereas the unoccupied $d_{x^2-y^2}$ orbital extends along [110] and $[1\bar{1}0]$. A corresponding OO could be expected for Mn^{2+} with both d_{z^2} and $d_{x^2-y^2}$ orbitals occupied. Our detailed electronic structure studies show that both d_{z^2} and $d_{x^2-y^2}$ orbitals are partially occupied for Mn^{2+} as well as Mn^{3+} as shown in Fig. 5. On the other hand, according to our charge-density analysis [Figs. 6(a) and 6(b)] the d_{z^2} orbital is ordered along the bc plane and $d_{x^2-y^2}$ orbital order along the ab plane for Mn(1) and Mn(2) (Fig. 7), which is consistent with experimental findings. Both d_{z^2} and $d_{x^2-y^2}$ orbitals are aligned in the same orientation within the layer as well as between the layers as shown in Fig. 7. So this type of OO is named F type.

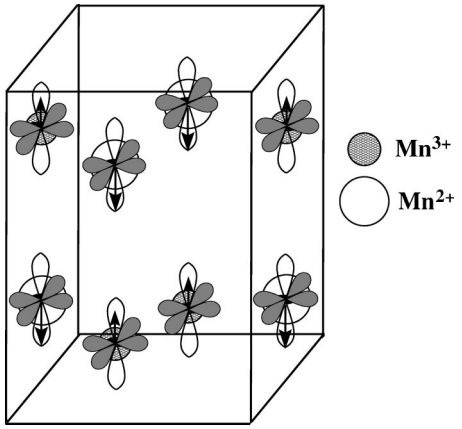

FIG. 7. Schematic diagram showing the checkerboard-type charge order (CO), F-type orbital order (OO), and G-type ferrimagnetic spin order (SO) of Mn in $YBaMn_2O_5$.

D. Optical properties

Further insight into the electronic structure can be obtained from the calculated interband optical functions. It has been earlier found that the calculated optical properties for SnI_2, $NaNO_2$, and MnX (X=As, Sb, Bi) (Refs. 44–46) are in excellent agreement with the experimental findings, and we have therefore used the same theory to predict the optical properties of $YBaMn_2O_5$. Since this material possesses unique Ferri ordering and semiconducting behavior along with a uniaxial crystal structure, it may find application in optical devices. Yet another reason for studying the optical properties is that it has been experimentally established[43] that the optical anisotropy of $Pr_{0.6}Ca_{0.4}MnO_3$ is drastically reduced above T_{CO}. It is therefore expected that the optical anisotropy will provide more insight into CO and OO in $YBaMn_2O_5$. For $YBaMn_2O_5$ with its tetragonal crystal structure, the optical spectrum is conveniently resolved into two principal directions $E\|a$ and $E\|c$, viz., with the electric field vector polarized along a and c, respectively. In the topmost panel of Fig. 8, the dispersive part of the diagonal elements of the dielectric tensor are given. The anisotropy in the dielectric tensor is clearly seen in this illustration.

In the second panel of Fig. 8, the polarized ϵ_2 spectra are shown. The spectra corresponding to $E\|a$ and $E\|c$ differ from one another up to ca. 10 eV whereas less difference is noticable in the spectra above 10 eV. Since there is a one-to-one correspondance between the interband transitions and band structures (discussed in Sec. IV A), we investigate the origin of the peaks in the ϵ_2 spectrum with the help of our calculated band structure. As $YBaMn_2O_5$ stabilizes in the Ferri state, the VB has an unequal number of bands in the up- and down-spin channels (Fig. 2), viz., 36 bands in the former and 38 in the latter. The two extra bands of the down-spin channel closer to E_F in the VB play an important role in

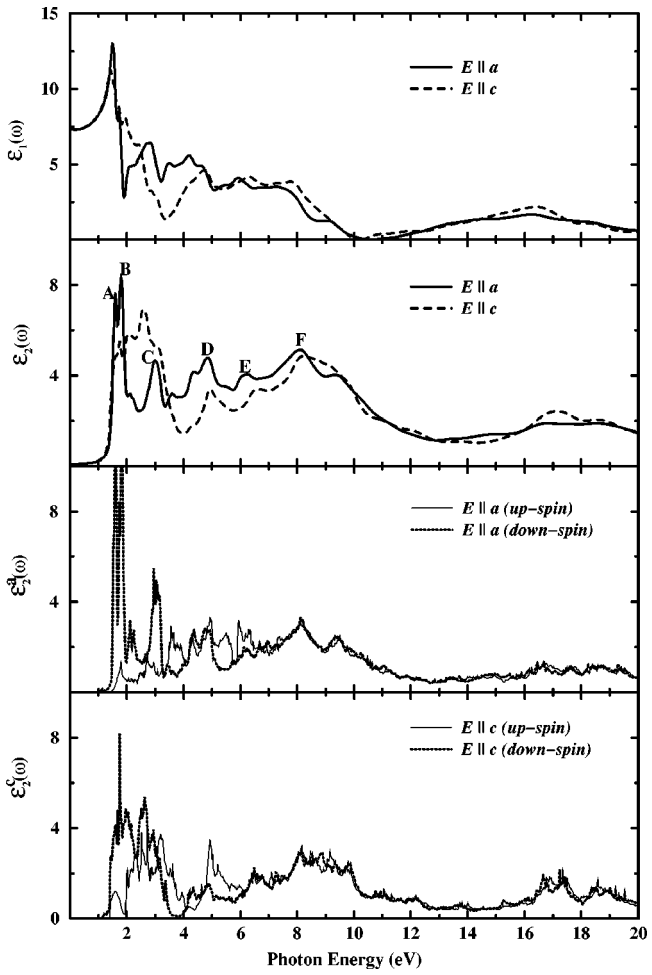

FIG. 8. Imaginary and real parts of the optical dielectric tensor of $YBaMn_2O_5$ are given in the first and second panels, respectively (note that the spectra are broadened). The spin-projected imaginary part of dielectric tensor along *a* and *c* directions are given in third and fourth panels, respectively.

the transitions as discussed below. We name the topmost band of the VB as No. 38 and bottommost band of the CB as No. 39. The lowest-energy peak *A* results from interband transitions [Nos. 35–41, mostly O(1) $2p$ to Mn(2) d_{z^2}, and Nos. 35–39, mostly Mn(1) d_{z^2} to Mn(2) $4p$] and peak *B* results from transitions (Nos. 38–48 and 36–49, mostly Mn $3d$ to Mn $4p$). Peak *C* originates from many transitions, including O $2p$ to Mn $3d$, Y $5s$ to Y $5p$, etc. Peaks *D*, *E*, and *F* are contributed by several transitions including O $2p$ to Mn $3d$ and Y $5s$ to Y $5p$. Further, a very small peak is present in the higher-energy region ($\sim$17 eV) of ϵ_2 which is due to transitions from lower-lying occupied levels to higher-lying unoccupied levels. The accumulation of broad Y $4d$ and Ba $5d$ bands in the high-energy part of the CB results in very little structure in the higher-energy part of the optical spectra. The optical gaps for $E\|a$ and $E\|c$ are approximately the same indicating that the effective intersite Coulomb correlation is the same for the in-plane and out-of-plane orientations for the Ferri phase. This can be traced back to the *G*-type Ferri coupling in this material.

In order to understand the origin of the optical anisotropy in $YBaMn_2O_5$ we have also made optical property calculations for the F phase, which show that (in contrast to the Ferri phase) the ϵ_2 spectrum for $E\|a$ is shifted some 3.5 eV to higher values than $E\|c$. Further, the ϵ_2 components of $E\|c$ for the F phase is much smaller than that for the Ferri phase, indicating that the large optical anisotropy in $YBaMn_2O_5$ is originating from the *G*-type Ferri ordering.

To emphasize the above finding, we have also plotted the spin-projected ϵ_2 spectra along the a [$\epsilon_2^a(\omega)$] and c [$\epsilon_2^c(\omega)$] directions (third and fourth panels of Fig. 8, respectively). Although the optical gap is approximately same for $E\|a$ and $E\|c$ in the ϵ_2 spectrum, there is a finite difference in the optical gaps related to up- and down-spin electrons in the $\epsilon_2^a(\omega)$ and $\epsilon_2^c(\omega)$ spectra. The optical gap for the down-spin case is smaller than that for up-spin case owing to the presence of the two narrow bands very close to E_F in the down-spin channel of the VB. There is a large difference between the spectra for up and down spins up to ca. 7 eV. The $\epsilon_2^a(\omega)$ spectrum resulting from the up-spin states has somewhat more dispersed peaks than that from down-spin states. The $\epsilon_2^a(\omega)$ spectrum resulting from the down-spin states has four well-defined peaks: two prominent peaks in the region 1.75–2 eV and two additional peaks at ca. 2.25 and 3 eV. The magnitude of the down-spin peaks are higher than those of the up-spin peaks in the $\epsilon_2^a(\omega)$ spectrum. The $\epsilon_2^c(\omega)$ spectrum originating from up- and down-spin states have appreciable differences up to ca. 6 eV. The down-spin part has two well-defined peaks at ca. 1.75 and 2.75 eV. The up-spin part has dispersed peaks of lower magnitude than the down-spin part, the magnitude of the up-spin peaks in $\epsilon_2^c(\omega)$ being generally higher than in $\epsilon_2^a(\omega)$. The optical anisotropy is noticeable in the direction- as well as spin-resolved ϵ_2 spectra. Hence, it is verified that the optical anisotropy originates both from crystal-field effects as well as from the Ferri ordering. As the reflectivity, absorption coefficient, and refractive index are often subjected to experimental studies, we have calculated these quantities and reproduced them in Fig. 9. We now advertice for experimental optical studies on $YBaMn_2O_5$.

E. XANES studies

X-ray absorption spectroscopy (XAS) has developed into a powerful tool for the elucidation of the geometric and electronic structure of amorphous and crystalline solids.[47] X-ray absorption occurs by the excitation of core electrons, which makes this technique element specific. Although the XANES only provides direct information about the unoccupied electronic states of a material, it gives indirect information about the valence of a given atom in its particular environment and about occupied electronic states. This is because the unoccupied states are affected by the occupied states through interaction with the neighbors.

The oxygen atoms are in two different chemical environments in $YBaMn_2O_5$ as clearly seen in PDOS in Fig. 4. The calculated *K*-edge spectra for O(1) and O(2) shown in Fig. 10 involve transition from the $1s$ core state to the unoccupied p state. In this context the Mn *K* edge mainly probes the

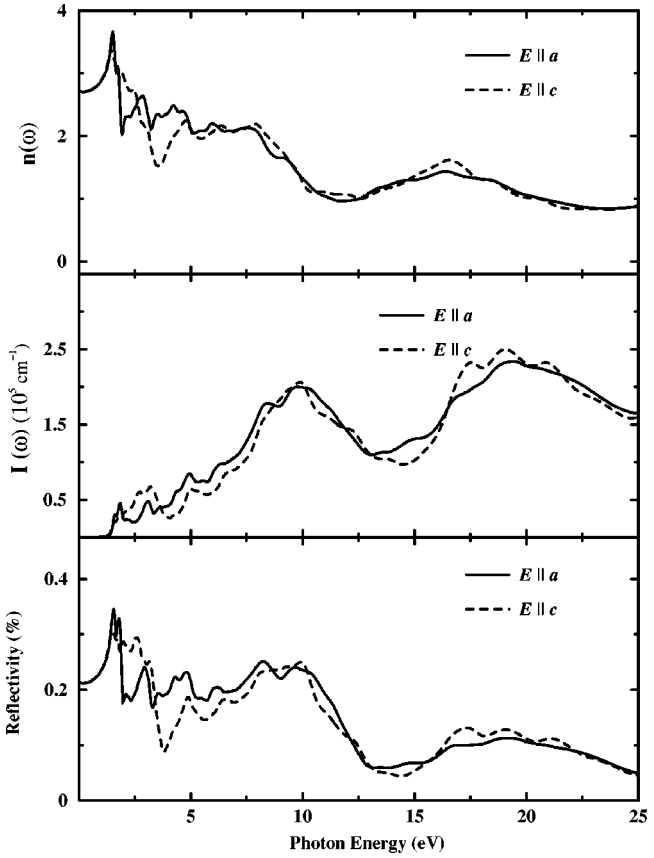

FIG. 9. Calculated reflectivity spectra, absorption coefficient $[(I(\omega)$ in 10^5 $\mathrm{cm}^{-1})]$ and refractive index $[n(\omega)]$ along a and c for $YBaMn_2O_5$.

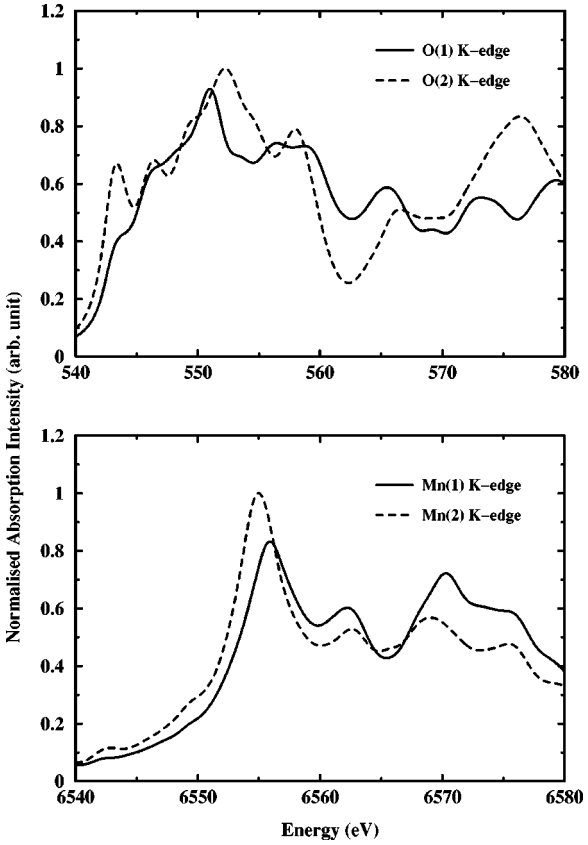

FIG. 10. Calculated K-edge spectra for Mn(1) and Mn(2) as well as O(1) and O(2) of $YBaMn_2O_5$.

unoccupied Mn $4p$ states. It is generally accepted that O K-edge spectra are very sensitive to the local structure of transition-metal oxides as documented for Fe_2O_3 (Ref. 48) and TiO_2 (Ref. 49). The K-edge spectra for O(1) and O(2) (Fig. 10) show appreciable differences throughout the whole energy range. In particular there are two peaks appearing in the O(2) spectrum between 540 and 550 eV that are absent for O(1). Within 3 Å, 2 Mn, 2 Y, and 6 O surround O(1) whereas, 2 Mn, 4 Ba, and 5 O surround O(2). It is this different chemical environment which causes the differences in the K-edge XANES spectra of O(1) and O(2).

$YBaMn_2O_5$ contains Mn in the valence states Mn^{3+} and Mn^{2+} which, as discussed in Sec. IV C, experience CO. An experimental technique to visualize CO is not available. In order to visualize the presence of different oxidation states for Mn, we have theoretically calculated the XANES K-edge spectra for Mn(1) and Mn(2) and presented them in Fig. 10. Both Mn atoms are seen to have four peaks within the energy range considered, reflecting that both are surrounded by five O within 2.08 Å. However, owing to the different valence states, there are intensity differences as well as energy shifts (some 1 eV) of these peaks. For example, the lower-energy peak has large intensity in the Mn(2) K-edge spectrum compared with that for Mn(1). On the contrary, the three higher-energy peaks in the Mn(2) K-edge spectrum are less intense than in the Mn(1) K-edge spectrum. When experimental XANES spectra become available for $YBaMn_2O_5$ the above features should be able to confirm the two different valence states for Mn.

F. Hyperfine parameters

The calculation of hyperfine parameters is useful to characterize different atomic sites in a given material. Many experimental techniques such as Mössbauer spectroscopy, nuclear magnetic and nuclear quadrupole resonance, and perturbed angular correlation measurements are used to measure hyperfine parameters. Hyperfine parameters describe the interaction of a nucleus with electric and magnetic fields created by its chemical environment. The resulting splitting of nuclear energy levels is determined by the product of a nuclear and an extra-nuclear quantity. In the case of quadrupole interactions, it is the nuclear quadrupole moment that interacts with the electric field gradient (EFG) produced by the charges outside the nucleus.[50] The EFG is a ground-state property of a material which depends sensitively on the asymmetry of the electronic charges. The direct relation of the EFG and the asphericity of the electron density in the vicinity of the probe nucleus enables one to estimate the quadrupole splitting and the degree of covalency or ionicity of the chemical bonds provided the nuclear quadrupole moment is known. Quantities describing hyperfine interactions (e.g., EFG and isomer shift) are widely studied nowadays both experimentally and theoretically.

TABLE II. Calculated (FLAPW method) principal component of the electric field gradient (EFG) V_{zz} in units of 10^{21} V/m^2 and the Fermi contact hyperfine field (HFF) in kG at the atomic sites in ferro- and ferrimagnetic configurations.

	Ferromagnetic		Ferrimagnetic	
Atom	EFG	HFF	EFG	HFF
Y	0.17	45.90	0.48	21.01
Ba	10.50	−19.24	10.08	38.85
Mn(1)	2.41	−73.36	0.09	−179.54
Mn(2)	−0.98	−210.98	1.01	318.79
O(1)	5.36	64.42	4.95	−42.59
O(2)	3.86	97.06	5.06	21.96

Blaha *et al.*[51] have showed that the linear augmented plane wave (LAPW) method is able to predict EFG's in solids with high precision. The charge distribution of complex materials such as $YBa_2Cu_3O_7$, $YBa_2Cu_3O_{6.5}$, and $YBa_2Cu_3O_6$ has been studied theoretically by Schwarz *et al.*[52] by this approach. In this study, we have attempted to establish the different valence states of Mn in $YBaMn_2O_5$ with the help of the EFG and the hyperfine field calculated using the FPLAPW method as embodied in the WIEN97 code.[30]

The total hyperfine field (HFF) can be decomposed in three terms: a dominant Fermi contact term, a dipolar term, and an orbital contribution. We limit our consideration to the contact term, which in the nonrelativistic limit is derived from the spin densities at the nuclear site:

$$H_c = \frac{8}{3}\pi\mu_B^2[\rho_\uparrow(0) - \rho_\downarrow(0)]. \tag{7}$$

The EFG is defined as the second derivative of the electrostatic potential at the nucleus, written as a traceless tensor. This tensor can be obtained from an integral over the nonspherical charge density $\rho(r)$. For instance the principal component V_{zz} is given by

$$V_{zz} = \int d^3r\rho(\mathbf{r})\frac{2P_2(\cos\theta)}{r^3}, \tag{8}$$

where P_2 is the second-order Legendre polynomial. A more detailed description of the calculation of the EFG can be found elsewhere.[53]

The calculated EFG and HFF at the atomic sites in $YBaMn_2O_5$ are given in Table II which confirm that there is a finite difference in the value of both the EFG and HFF between the two Mn atoms. So we can conclude that their charge distribution is quite different. The higher value of the EFG and HFF in Mn^{2+} than in Mn^{3+} is justified because more charge is found on the latter. This can be seen from the orbital-projected DOS as well as from the magnetic moments possessed by the two ions. The HFF for Mn^{3+} in $LaMnO_3$ is found to be −198 kG,[36] which is quite close to −179 kG found for Mn^{3+} in our case. Consequently we substantiate that Mn(1) corresponds to Mn^{3+}. The two oxygen ions also differ mutually in their values for the EFG and HFF (Table II), suggesting that the strength of the covalent bond formed by them with Mn(1) and Mn(2) is different.

V. SUMMARY

Like hole-doped $RMnO_3$-based CMR materials $YBaMn_2O_5$ also carries mixed-valence states of manganese, ferrimagnetic ordering, and charge ordering and apparently undergoes a combined insulator-to-metal and ferrimagnetic-to-ferromagnetic transition. Hence $YBaMn_2O_5$ may be a potential CMR material which deserves more attention.

We have made a detailed investigation of the electronic properties of $YBaMn_2O_5$ using the full-potential LMTO method as well as the full-potential LAPW method and conclude the following.

(i) The *G*-type ferrimagnetic semiconducting state is found to be the ground state in accordance with experimental findings.

(ii) The existence of the two different types of Mn atoms is visualized by differences in site- and orbital-projected DOS curves. In order to further emphasize the different valence states of Mn, we have calculated *K*-edge XANE spectra. For Mn as well as O the existence of two types of valence-induced atomic species is established with the help of *K*-edge spectra.

(iii) The occurrence of checkerboard-type charge ordering and F-type orbital ordering is seen from the charge-density plots. The small size of Y^{3+} makes the Mn-O-Mn bond angle deviate from 180°, which in turn imposes a reduction in the e_g bandwidth. The charge- and orbital-ordering features are believed to result from this perturbation of the e_g orbitals.

(iv) As $YBaMn_2O_5$ is a ferrimagnetic semiconductor, it is useful to probe its optical properties for potential applications. We have analyzed the interband contributions to the optical properties with the help of the calculated electronic band structure features. We found large anisotropies in the optical spectra originating from ferrimagnetic ordering and the crystal field splitting. No experimental optical study of $YBaMn_2O_5$ is hitherto available.

(v) Hyperfine parameters such as hyperfine field and electric field gradients have also been calculated showing very large differences in the computed values for the crystallographically different manganese and oxygen atoms. This substantiates that Mn exists in two different valence states in $YBaMn_2O_5$.

ACKNOWLEDGMENTS

This work has received support from The Research Council of Norway (Program for Supercomputing) through a grant of computing time. R.V. wishes to thank Professor John Wills, Professor Peter Blaha, and Professor Karlheinz Schwarz for supplying their computer codes used in this study and Professor Olle Eriksson for useful communications. R.V. kindly acknowledges Professor L. Veseth and P. Vajeeston for useful discussions.

*Electronic address: ravindran.vidya@kjemi.uio.no

[1] A. Fujimori, T. Mizokawa, and T. Saitoh, in *Colossal Magnetoresistance, Charge Ordering and Related Properties of Manganese Oxides*, edited by C.N.R. Rao and B. Reveau (World Scientific, Singapore, 1998), p. 279.
[2] R. Mahendiran, A.K. Raychaudhuri, A. Chainani, D.D. Sarma, and S.B. Ray, Appl. Phys. Lett. **66**, 233 (1995).
[3] J.Z. Liu, I.C. Chang, S. Irons, P. Klavins, R.H. Shelton, K. Song, and S.R. Wasserman, Appl. Phys. Lett. **66**, 3218 (1995).
[4] G.Q. Gong, C. Canedy, G. Xiao, J.Z. Sun, A. Gupta, and W.J. Gallagher, Appl. Phys. Lett. **67**, 1783 (1995).
[5] V. Caignaert, A. Maignan, and B. Raveau, Solid State Commun. **95**, 357 (1995).
[6] N. Furukawa, J. Phys. Soc. Jpn. **63**, 3214 (1994); Y. Tokura, A. Urushibara, Y. Moritomo, T. Arima, A. Asamitsu, G. Kido, and N. Furukawa, *ibid.* **63**, 3931 (1994).
[7] A.J. Millis, P.B. Littlewood, and B.I. Shraiman, Phys. Rev. Lett. **74**, 5144 (1995).
[8] M.A. Dixon, Physica C **174**, 117 (1991).
[9] J.B. Torrance, A. Bezinge, A.I. Nazzal, T.C. Huang, S.S.P. Parkin, D.T. Keane, S.L. La Placa, P.M. Horn, and G.A. Held, Phys. Rev. B **40**, 8872 (1989).
[10] H. Kuwahara and Y. Tokura, in *Colossal Magnetoresistance, Charge Ordering and Related Properties of Manganese Oxides* (Ref. 1), p. 217.
[11] Y. Moritomo, A. Asamitsu, H. Kuwahara, and Y. Tokura, Nature (London) **380**, 141 (1996).
[12] J.P. Chapman, J.P. Attfield, M. Mölgg, C.M. Friend, and T.M. Beales, Angew. Chem. Int. Ed. Engl. **35**, 2482 (1996).
[13] T. Vogt, P.M. Woodward, P. Karen, B.A. Hunter, P. Henning, and A.R. Moodenbaugh, Phys. Rev. Lett. **84**, 2969 (2000).
[14] Y. Tokura and N. Nagaosa, Science **288**, 462 (2000).
[15] C. Martin, A. Maignan, D. Pelloquin, N. Nguyen, and B. Raveau, Appl. Phys. Lett. **71**, 1421 (1997).
[16] V.I. Anisimov, I.S. Elfimov, M.A. Korotin, and K. Terakura, Phys. Rev. B **55**, 15 494 (1997).
[17] W. Koshibae, Y. Kawamura, S. Ishihara, and S. Okomoto, J. Phys. Soc. Jpn. **66**, 957 (1997).
[18] T. Mizokawa and A. Fujimori, Phys. Rev. B **56**, R493 (1997).
[19] J. Lee, J. Yu, and K. Terakura, J. Korean Phys. Soc. **33**, S55 (1998).
[20] I. Solovyev, N. Hamada, and K. Terakura, Phys. Rev. Lett. **76**, 4825 (1996).
[21] J.D. Lee and B.I. Min, Phys. Rev. B **55**, R14 713 (1997).
[22] P. A. Cox, *Transition Metal Oxides* (Clarendon, Oxford, 1992); E.J.W. Verwey and P.W. Haayman, Physica (Amsterdam) **8**, 979 (1941).
[23] J. Linden, P. Karen, A. Kjekshus, J. Miettinen, T. Pietari, and M. Karppinen, Phys. Rev. B **60**, 15 251 (1999).
[24] J.A. McAllister and J.P. Attfield, Mater. Sci. Forum **278-281**, 744 (1998).
[25] F. Millange, E. Suard, V. Caignaert, and B. Raveau, Mater. Res. Bull. **34**, 1 (1999).
[26] J. M. Wills (unpublished); J.M. Wills and B.R. Cooper, Phys. Rev. B **36**, 3809 (1987); D.L. Price and B.R. Cooper, *ibid.* **39**, 4945 (1989).
[27] O.K. Andersen, Phys. Rev. B **12**, 3060 (1975).
[28] D.J. Chadi and M.L. Cohen, Phys. Rev. B **8**, 5747 (1973); S. Froyen, *ibid.* **39**, 3168 (1989).
[29] J. P. Perdew, in *Electronic Structure of Solids*, edited by P. Ziische and H. Eschrig (Akademie Verlag, Berlin, 1991), p. 11; J.P. Perdew, K. Burke, and Y. Wang, Phys. Rev. B **54**, 16 533 (1996); J.P. Perdew, K. Burke, and M. Ernzerhof, Phys. Rev. Lett. **77**, 3865 (1996).
[30] P. Blaha, K. Schwarz, and J. Luitz, computer code WIEN97, Vienna University of Technology, 1997 [an improved and updated Unix version of the original copyrighted code published by P. Blaha, K. Schwarz, P.I. Sorantin, and S.B. Trickey, Comput. Phys. Commun. **59**, 399 (1990)].
[31] D. Singh, Phys. Rev. B **43**, 6388 (1991).
[32] P.E. Blöchl, O. Jepsen, and O.K. Andersen, Phys. Rev. B **49**, 16 223 (1994).
[33] N.V. Smith, Phys. Rev. B **3**, 1862 (1971).
[34] M. Alouani and J.M. Wills, Phys. Rev. B **54**, 2480 (1996).
[35] T.P. Beales, M. Mölgg, J. Jutson, and C.M. Friend, Phys. Status Solidi A **161**, 271 (1997).
[36] P. Ravindran, A. Kjekshus, H. Fjellvågr, A. Delin, and O. Eriksson, Phys. Rev. B **65**, 064445 (2002).
[37] J.B. Goodenough, *Magnetism and the Chemical Bond* (Wiley, New York, 1963).
[38] H. Sawada and K. Terakura, Phys. Rev. B **58**, 6831 (1998).
[39] J.B. Goodenough, Phys. Rev. **100**, 564 (1955); J. Kanamori, J. Phys. Chem. Solids **10**, 87 (1959).
[40] C.N.R. Rao and A. K. Raychauduri, in *Colossal Magnetoresistance, Charge Ordering and Related Properties of Manganese Oxides* (Ref. 1), p. 1.
[41] Y. Tokura, H. Kuwahara, Y. Moritomo, Y. Tomioka, and A. Asamitsu, Phys. Rev. Lett. **76**, 3184 (1996).
[42] S.-W. Cheong, in *Colossal Magnetoresistance, Charge Ordering and Related Properties of Manganese Oxides* (Ref. 1), p. 241.
[43] Y. Okimoto, Y. Tomioka, Y. Onose, Y. Otsuka, and Y. Tokura, Phys. Rev. B **57**, R9377 (1998).
[44] P. Ravindran, A. Delin, R. Ahuja, B. Johansson, S. Auluck, J.M. Wills, and O. Eriksson, Phys. Rev. B **56**, 6851 (1997).
[45] P. Ravindran, A. Delin, B. Johansson, O. Eriksson, and J.M. Wills, Phys. Rev. B **59**, 1776 (1999).
[46] P. Ravindran, A. Delin, P. James, B. Johansson, J.M. Wills, R. Ahuja, and O. Eriksson, Phys. Rev. B **59**, 15 680 (1999).
[47] P. Behrens, TrAC, Trends Anal. Chem. **11**, 218 (1992).
[48] J.H. Paterson and O.L. Krivanek, Ultramicroscopy **32**, 313 (1990).
[49] V.S. Lusvardi, M.A. Barteau, J.G. Chen, J. Eng Jr., and A.V. Teplyakov, Surf. Sci. **397**, 237 (1998).
[50] H.M. Petrilli, P.E. Blöchl, P. Blaha, and K. Schwarz, Phys. Rev. B **57**, 14 690 (1998).
[51] P. Blaha, K. Schwarz, and P. Herzig, Phys. Rev. Lett. **54**, 1192 (1985).
[52] K. Schwarz, C. Ambrosch-Draxl, and P. Blaha, Phys. Rev. B **42**, 2051 (1990).
[53] P. Blaha, K. Schwarz, and P.H. Dederichs, Phys. Rev. B **37**, 2792 (1988); C. Ambrosch-Draxl, P. Blaha, and K. Schwarz, **44**, 5141 (1991); K. Schwarz and P. Blaha, Z. Naturforsch., A: Phys. Sci. **47**, 197 (1992).